

# Solar Pumping of Fiber Lasers with Solid-State Luminescent Concentrators: Design Optimization by Ray Tracing

Stephan Dottermusch, Taizo Masuda, Masamori Endo, Bryce S. Richards, and Ian A. Howard\*

Solar-pumped lasers (SPLs) typically couple sunlight into the laser cavity using focusing optics and solar tracking. Luminescent solar concentrators (LSC) are an alternative, fully planar, scalable pump source that can concentrate diffuse light. For liquid LSC-based SPLs, reflective cavities have been used to trap light and pump a Nd<sup>3+</sup>-doped silica fiber. Here, three solid-state LSC-based SPL designs, in addition to the reflective cavity making use of total internal reflection, are analyzed by ray-tracing simulations. Results are compared to a liquid LSC reference, also used for validating simulations. Substituting the liquid-state LSC for a solid-state LSC (with the fiber placed inside) allows a 7-fold enhancement of the gain coefficient, corresponding to a 30-fold enhancement of the laser output power. An additional 4-fold increase of the output power is possible with a fiber of kilometers length. These results show a roadmap for realizing SPLs with output powers on the order of 2.8 W m<sup>-2</sup> under terrestrial sunlight, while keeping an identical reflective cavity used for the liquid LSC design. In addition, room-temperature operation should be possible with certain solid LSC designs, and the necessity for a reflective cavity comprised of costly dielectric mirrors may be relieved.

## 1. Introduction


The conversion of incoherent sunlight into a coherent laser beam has captured scientific interest for more than half a

Dr. S. Dottermusch, Prof. B. S. Richards, Dr. I. A. Howard  
Institute of Microstructure Technology (IMT)  
Karlsruhe Institute of Technology (KIT)  
Eggenstein-Leopoldshafen 76344, Germany  
E-mail: ian.howard@kit.edu

Dr. T. Masuda  
R-Frontier Division  
Toyota Motor Corporation  
Susono, Shizuoka, Japan

Dr. T. Masuda  
Institute for Advanced Science  
The University of Electro-Communications  
Tokyo, Japan

Prof. M. Endo  
Department of physics  
Tokai University  
Kanagawa, Japan

 The ORCID identification number(s) for the author(s) of this article can be found under <https://doi.org/10.1002/adom.202100479>.

© 2021 The Authors. Advanced Optical Materials published by Wiley-VCH GmbH. This is an open access article under the terms of the Creative Commons Attribution License, which permits use, distribution and reproduction in any medium, provided the original work is properly cited.

DOI: 10.1002/adom.202100479

century, with the first solar-pumped laser (SPL) being demonstrated in the early 1960s.<sup>[1]</sup> Like this first system, most SPLs today rely on curved mirrors, lenses, or a combination of the two, for focusing incident sunlight into the gain material, typically an Nd:YAG or Cr,Nd:YAG rod,<sup>[2]</sup> to achieve population inversion. Concentration factors of several thousand can be reached in such designs. It is possible to distinguish two focusing schemes: i) in end-pumping, the focused sunlight is introduced to the laser cavity through one of the end mirrors;<sup>[3,4]</sup> and ii) in side-pumping, the light pumps the gain medium transversely to the resonator direction.<sup>[5,6]</sup> The advantages of side-pumping include a reduced need for system cooling (due to a more homogeneous absorption along the gain medium),<sup>[7]</sup> higher laser beam quality (brightness),<sup>[8]</sup> and increased scalability

(by simply expanding the gain volume).<sup>[9]</sup> The highest laser brightness was achieved in TEM<sub>00</sub> operation of side-pumped systems.<sup>[10,11]</sup> A key challenge in side-pumping is the shorter optical pathlength through the gain medium compared to end-pumping. Many powerful systems today, combine end-pumping and side-pumping of gain crystals.<sup>[12–14]</sup> The highest efficiency achieved is 32.5 W output power per m<sup>2</sup> collection area under 870 W m<sup>-2</sup> solar irradiance on the test day.<sup>[14]</sup>

SPLs have attracted much attention because they have a wide range of potential applications. The above-mentioned conventional approaches rely on the focusing of sunlight using lenses or mirrors, requiring precise sun-tracking, and therefore resulting in large, expensive, and heavy systems. On this large scale, taking advantage of MW scale solar furnaces could allow SPLs with 20 kW output powers.<sup>[15]</sup> An application for an SPL in this power range has been proposed in terms of the renewable Mg/MgO energy cycle, where the laser light from the SPL is used to reduce MgO at 4000 K.<sup>[16]</sup> Lighter, compact, and more reliable systems are of value when it comes to other potential applications for SPLs, such as power transmission,<sup>[17,18]</sup> space propulsion,<sup>[19]</sup> and communication in space,<sup>[20,21]</sup> or wireless power transmission to electrical vehicles.<sup>[22]</sup> More compact systems are possible based on radiative energy transfer.<sup>[23]</sup>

In systems making use of radiative energy transfer, sunlight is absorbed by a luminescent material whose photon emission enables an energy transfer into the optical gain medium of the laser. The basic idea is to utilize a larger absorption volume of

luminescent material and concentrate its emitted light into a smaller volume occupied by the optical gain material. Luminescent solar concentrators (LSCs), in which emitted light from luminescence centers is transported within a thin slab due to total internal reflection (TIR), were originally introduced as a solar energy harvesting technology in the mid-1970s.<sup>[24]</sup> Additionally to the more compact and fully-planar design, LSCs exhibit a key advantage over other solar concentrator technologies in that they are able to effectively concentrate diffuse light,<sup>[25]</sup> often occurring under cloudy skies, leading to an overall higher potential in energy output compared to system only relying on direct sunlight.<sup>[26]</sup>

Previously, a functional SPL has been shown, based on a radiative energy transfer from a luminescent dye in solution, that does not require lenses, or mirrors, and solar tracking systems.<sup>[27]</sup> To realize this liquid-LSC SPL, 190 m of Nd<sup>3+</sup>-doped optical fiber were coiled into a light-trapping chamber (Ø300 mm, 1.5 mm thickness). The chamber was filled with a 0.3 mmol L<sup>-1</sup> solution of Rhodamine 6G (R6G) dye in methanol. Sunlight entered the chamber through a fused silica plate coated with a dichroic mirror. The rear side, and edges of the chamber were also coated with dielectric mirrors. A picture of the methanol filled chamber, with the 190 m long silica fiber inside it, is available in the Supporting Information (Figure S1). Due to the optical contact of the solution with the dichroic mirror and walls, light was not trapped by TIR in the liquid, but only prevented from escaping due to the reflectance of the mirrors. Trapping by dielectric mirrors introduces losses that

are strongly dependent upon the incidence angle of light on the interface.<sup>[28]</sup> For example, perfect reflectance is not possible when employing a common SiO<sub>2</sub>/TiO<sub>2</sub> dielectric layer stack at a methanol interface. At an incidence angle of 74° from methanol, light passes through the layer stack at the Brewster angle between SiO<sub>2</sub> and TiO<sub>2</sub>. Under this condition, *p*-polarized light is not reflected at all. Nevertheless, lasing at 1064 nm with a maximum power output of 0.018 W m<sup>-2</sup> collection area was achieved under 1-sun illumination when the system was cooled to -25 °C to reduce intrinsic losses in the silica fiber.<sup>[29]</sup>

The key advantage when moving from the liquid to a solid LSC design is the introduction of TIR to the system. A thin-film LSC, based on a doped polymer layer on a fused silica substrate of 300 mm diameter, produced in our laboratory is pictured in Figure 1a, with the concentrated edge emission clearly visible even under laboratory lighting. Unlike the solar cells attached around the perimeter of an LSC for photovoltaic applications, the doped silica fiber is a weak and narrow-band absorber. These substantially different properties of the absorbing fiber place unique requirements on the LSC; the requirements for the LSC are altered compared to those optimized to pump photovoltaic cells. Thus, although the knowledge gained from the extensive study of LSCs for photovoltaic applications over the last four decades is useful,<sup>[30,31]</sup> the unique requirements of the SPL system require considerable redesign and optimization.

The first unique factor to consider, the weak absorption in the doped silica fiber, is a result of the limited doping capacity of silica with Nd<sup>3+</sup>.<sup>[33]</sup> Nevertheless, to date, Nd<sup>3+</sup> is one of

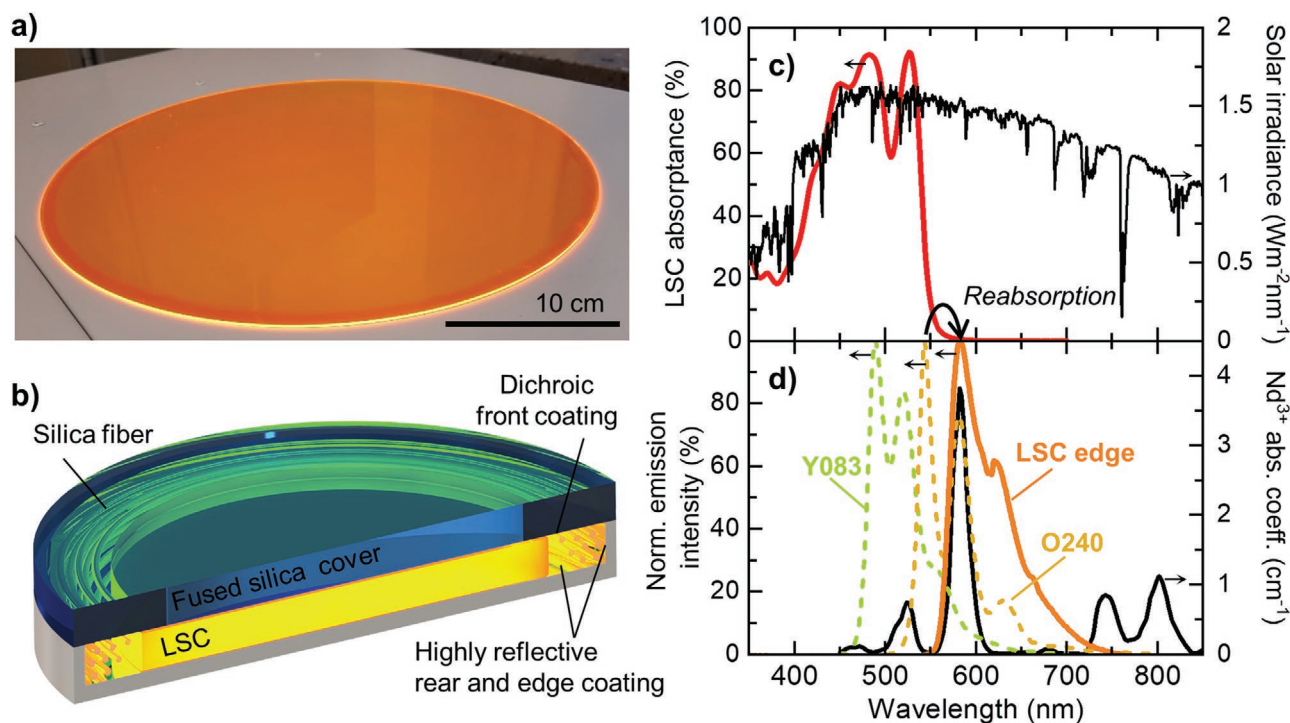


**Figure 1.** a) Photograph of a 300 mm diameter exemplary LSC fabricated by coating a fused silica plate with a polymer layer containing the perylene-based dyes Lumogen F O240 (O240) and Lumogen F Y083 (Y083). b) Illustration of the LSC in a chamber with reflective surfaces based on dielectric-coatings. c) Measured absorbance of the exemplary LSC, as well as the air-mass 1.5 global (AM1.5g) solar irradiance spectrum.<sup>[32]</sup> d) Normalized emission intensity of the dyes contained in the LSC and the measured edge emittance of the LSC, as well as the absorption coefficient of Nd<sup>3+</sup> doped silica fiber core.

the best available dopants for achieving lasing under modest pumping due to its four-level system. A four-level system allows the low losses that are needed to compensate for the comparably low pump power densities in the SPL system.<sup>[29]</sup> The following uses ray tracing to study the replacement of the dye-solution with a variety of solid LSC SPL designs. The surrounding reflective light trapping chamber is maintained to counteract the weak fiber absorption. The solid LSC, along with a silica fiber, inside the light-trapping chamber is illustrated in Figure 1b. Compared to photovoltaic applications in a system of similar dimensions the average optical pathlength is much longer. The longer pathlength means that loss mechanism such as the host absorption, the scattering of light, and the reabsorption of light, must play more pronounced roles than in LSCs used to pump solar cells.

The reabsorption is especially important considering the narrow absorption bands of  $\text{Nd}^{3+}$ . With the dye concentration the absorbance of incident light increases, but so does the reabsorption. Reabsorption red shifts the spectrum in the LSC, and it is especially important to match the red-shifted spectrum to the  $\text{Nd}^{3+}$  absorption band. Thus an optimum concentration exists, based on the absorbance of incident light and reabsorption in the LSC.<sup>[34]</sup> Due to the long pathlength, the dye absorption tail is of high importance in this respect. Next to R6G (used in the dye-solution work), the perylene-based dye Lumogen F O240 (O240) has proven a suitable candidate for pumping a  $\text{Nd}^{3+}$  absorption band (the  ${}^4\text{G}_{5/2}$ - ${}^2\text{G}_{7/2}$  band). This is shown in Figure 1b,c. Figure 1b shows the absorbance spectrum of the example LSC in Figure 1a, overlaid with the air-mass 1.5 global (AM1.5g) solar irradiance spectrum.<sup>[32]</sup> In addition to O240 the LSC is doped with Lumogen F Y083 (Y083), to expand the absorption range. The dye concentration was optimized to reach a single pass peak optical density of one for both dyes. At this optical density, the absorption of incident light in the wavelength range 550 nm to 600 nm is negligible, but reabsorption of light on the long pathlengths within the LSC leads to a significant red-shifted LSC edge emission spectrum overlapping well with the  $\text{Nd}^{3+}$  absorption peak at 590 nm (Figure 1d). Thus, the absorption tail is an important part in determining the suitability of a fluorophore in this scheme.

In the following, ray-tracing simulations consider what fraction of the incident solar power can be absorbed by the  $\text{Nd}^{3+}$  ions in the fiber in different designs. Key results are the quantification of potential improvements in SPL performance, determining which design is best suited for SPL operation at a specific temperature, and establish the needed conditions to operate the SPL without the dielectric coatings. The paper is structured as follows: First, the designs and the parameters for the numerical simulations are introduced. Then, the efficiency of power transfer to the  $\text{Nd}^{3+}$ -doped silica fiber is determined; the designs are compared to the reference dye-solution-based SPL (mentioned in the introduction and that from now on will be referred to as the “reference design”).<sup>[27]</sup> The loss mechanisms, in each case, are explored. Thereafter, the optimum design and silica fiber length are determined as a function of the temperature-dependent silica fiber losses. Finally, the performance drop upon removal of the dielectric coatings in the light-trapping chamber is determined, and which designs can minimize this loss considered.

## 2. Solid-State LSC Designs & Simulation Parameters

In photovoltaics the solar cells pumped by the LSC are brought into optical contact with the edges of the LSC. In the SPL, the placement of the silica fiber with respect to the LSC is less trivial. One goal of this work is to determine the best suitable design for placing the silica fiber. The key criterion is the photon density (within the  $\text{Nd}^{3+}$  absorption band) at the position of the silica fiber, as this directly determines the power absorbed by the fiber. Three designs for the solid LSC were conceived and compared to the reference design, all four design are illustrated in Figure 2 in a cross-sectional view. Additionally,

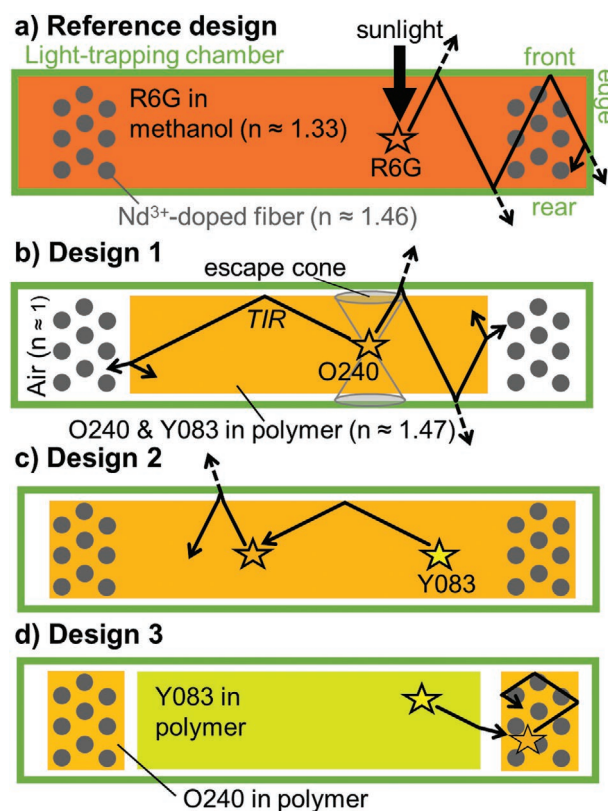


**Figure 2.** Cross-sectional illustrations of the SPL designs under investigation, as well as important mechanisms for the propagation of light in the systems. a) Reference design of an SPL with a liquid-based LSC making use of Rhodamine 6G (R6G) in methanol. In this system emitted light only propagates towards the  $\text{Nd}^{3+}$ -doped silica fiber by lossy reflection on the front- and rear surface of the dielectric-based light-trapping chamber. b) Solid LSC Design 1, with silica fiber wrapped around the edge of an LSC containing the dyes Lumogen F O240 (O240) and Lumogen F Y083 (Y083). Light emitted outside the escape cone (critical angle  $\sim 43^\circ$ ) propagates inside the LSC via TIR, while luminescence inside the escape cone propagates by lossy reflection on the chamber surfaces. At the edge of the LSC light is partially reflected. c) Solid LSC Design 2, makes use of the light reflected at the LSC edge, by incorporating the silica fiber within the LSC. In all solid designs reabsorption events and scattering events can change the propagation angle and with it the propagation mechanism. d) Solid LSC Design 3, incorporates the silica fiber within a ring LSC (doped with O240) pumped by a central disc LSC (doped with Y083), separated by an air gap. The trapping of light inside the small volume of the ring LSC leads to high photon densities.

the most important mechanisms for light propagation in the systems are shown in the figure.

Figure 2a shows the *reference design*. Incident light is absorbed and emitted by R6G. The emitted light propagates by reflection from the front (dichroic mirror) and rear (dielectric mirror) surfaces of the light-trapping chamber. With every incidence event there is a chance of losing light as the angular and polarization-dependent reflectance is not unity. The same is true when light reaches the edge of the light-trapping chamber.

*Design 1*, presented in Figure 2b, is the technically simplest design for an SPL employing a solid LSC. The silica fiber is wrapped around the edge of the solid LSC containing the dyes O240 and Y083. Light emitted inside the escape cone propagates by reflection on the surfaces of the light-trapping chamber. Light emitted outside the escape cone propagates on the basis TIR. Furthermore, at the edge of the LSC light can escape to reach the fiber, or be reflected and remain with the LSC.

The reflection of light at the edge of the LSC leads to higher photon density inside the LSC compared to the outside. *Design 2*, presented in Figure 2c, utilizes these higher photon densities, by placing the silica fiber inside the LSC. Additionally, the design reduces the reliance of the system on the light-trapping chamber, since the photon density near the fiber is increased due to the light trapped by TIR even in the absence of the light-trapping chamber. In this regard, it is important to keep in mind that events like reabsorption and scattering, can change the propagation angle of light. Reabsorption occurs over short and long distances. Within a few millimeters, light emitted at a wavelength < 550 nm is reabsorbed by Y083 or by O240. Light emitted at wavelengths longer than 550 nm is reabsorbed within several centimeters by O240. Exemplarily, Figure 2c illustrates light at first propagating outside the escape cone, after being emitted by Y083, and then propagation inside the escape cone after a reabsorption event involving O240. Scattering events occur in bulk materials, at impurities, and at optical interfaces.

To further increase the photon density, *Design 3* (Figure 2d) makes use of a two-stage cascade energy transfer. The silica fiber is placed in a ring LSC containing O240. Higher photon density in the region of the fiber in the ring LSC is expected due to its reduced volume compared to that of the disc LSC (this cascade trapping is illustrated in Figure 2d). The central disc LSC in Design 3 only contains Y083 to match the edge emission spectrum to the excitation spectrum of the ring LSC contain the silica fiber. Hence a drawback to this design is a reduced absorption of incident solar light (due to the more limited absorption range of the single dye).

The illustrations in Figure 2 closely relate to the simulation work presented in the following. Although, as an example, a thin-film LSC on a fused silica substrate is shown in Figure 1a, simulations are based on thick-films. Whether a thin or thick film configuration is targeted for eventual experimental realization does not impact on this comparison of the designs. Equivalent properties in terms of absorption, reabsorption, and scattering could be reached in both thin, and thick film implementations. Ultimately the choice between these two should be made with regard to practical challenges in realizing the different designs.

The ray-tracing-based program LightTools (Synopsis) was used to define the geometry and materials, and to perform the simulations. Full details on the implemented geometry are discussed in the Methods (Section 5) below. The implemented simulation parameters, are based on measurements performed with a fluorinated polyurethane host, employing the two dyes O240 and Y083. Furthermore, the excitation and emission spectra of R6G in methanol was measured to model the reference design. Details on the fabrication and measurement procedures, as well as utilized devices, are available in the Methods (Section 5) below. All wavelength-dependent measurement results are available in the Supporting Information (Figure S2 and Figure S3). Measured parameters of the polyurethane host include the absorption coefficient ( $3.5 \times 10^{-3} \text{ cm}^{-1}$  at 600 nm), the scattering coefficient ( $10^{-1} \text{ cm}^{-1}$  at 600 nm), and the refractive index (1.47 at 637 nm). The close match with the refractive index of fused silica (1.46 at 600 nm)<sup>[35]</sup> was one reason for choosing fluorinated polyurethane as the host material. Given the similar index of the polymer host and the cladding of the silica fiber, scattering at the polymer/cladding interface nearly vanishes when the fiber is embedded. We note that embedding the fiber in the LSC does not affect the waveguiding of the laser light in the core of the fiber (due to the index difference between the core and cladding of the fiber). Furthermore, the absorption tail of O240 within the polyurethane host (see Figure S3b) proved suitable for achieving a good overlap of the LSC emission spectrum with the Nd<sup>3+</sup> absorption spectrum (see Figure 1d). The absorption coefficient of the Nd<sup>3+</sup>-doped silica fiber core, also implemented in simulations, was obtained from transmittance measurements.<sup>[27]</sup> With a peak in the absorption coefficient of  $3.8 \text{ cm}^{-1}$  at a wavelength of 582 nm, the single pass absorption of the silica fiber (16  $\mu\text{m}$  core diameter) is small (< 0.6%). The low scattering and absorption from the fibers embedded in an appropriate LSC leads to a homogeneous light density in the LSC and consequently a uniform pumping of the entire length of the fiber. The reflectance of the dielectric coatings of the light-trapping chamber were calculated and optimized using the program TFCalc (Software Spectra, Inc.) based on a total of 80 layers of SiO<sub>2</sub> and TiO<sub>2</sub>. The utilized reflectance values are available in the Supporting Information (Figure S5, and Figures S7–S9).

## 3. Results and Discussion

### 3.1. Losses in the Assorted Designs

The key figure-of-merit in the numerical simulations was the power absorbed by Nd<sup>3+</sup> ions, as this is the most robustly extractable parameter from the LightTools software package for volumes and surfaces. Although, the rate of photon absorption in the silica fiber is physically the critical parameter for lasing, the absorbed power is more accessible in this software tool. Also, due to the narrow Nd<sup>3+</sup> absorption band, a linear relationship between the pump rate and the power absorbed exists, so pumping rates of the Nd<sup>3+</sup> can be obtained from this power-based analysis.

For all simulations, uniform normal-incidence, collimated light was incident from a 300 mm diameter source aligned to

illuminate the LSC, resulting in a constant incident power of 70.07 W impinging on the system. In the following, a power balance is shown for each design, and loss mechanisms are discussed in detail. External, internal, and conversion losses can be distinguished. External losses prevent the absorption of incident light by the fluorophore in the LSC. External losses are further separated into:

1. *Spectral mismatch loss.* Light outside the absorption range of the fluorophores employed in the LSC cannot be absorbed and is lost. For Designs 1 and 2, as well as for the reference design, the absorption range is defined to be  $< 550$  nm, whereas for Design 3 the absorption range is only  $< 500$  nm.

2. *Non-absorption loss.* Not all light in the absorption range is absorbed. A fraction of the incident light is reflected at the interfaces above the LSC or passes through the LSC, is reflected, passes through the LSC again and escapes without being absorbed (due to a small optical density at the respective wavelength).

Conversion losses are losses related to the absorption and emission process by the dyes. Conversion losses are further separated into:

3. *Stokes-shift loss.* A loss in power occurs as absorbed photons are emitted at a longer wavelength. This loss appears in the power-related discussion but is not relevant for the photon flux pumping the gain medium. This “loss” channel in terms of power need not be minimized.

4. *Non-unity PLQY loss.* All dyes (R6G, O240 and Y083) are known for their high photoluminescent quantum yields (PLQY),<sup>[36,37]</sup> hence a PLQY of 95% was assumed for all dyes. However, with the multiple cycles of reabsorption and re-emission, the loss due to the non-unity PLQY can make a non-negligible contribution.

Internal losses prevent the light emitted by the dyes from being absorbed by the  $\text{Nd}^{3+}$  ions. Internal losses are separated into:

5. *Dielectric coating loss.* Together, the dielectric coatings on the front and rear surface enable the reflection-based propagation of light inside the chamber (see Figure 2a). All light escaping through the front- and rear dielectric coatings is assumed to be lost in simulations. The argument here: the dielectric coatings are highly effective mirrors, the fraction of light reentering the system is negligible, even when a metallic mirror is placed below the chamber.

6. *Edge loss.* In simulations a reflectance of 45% is used for the edge surface of the light-trapping chamber (see Figure 2a) in accordance with the reference design.<sup>[27]</sup>

7. *Parasitic absorption loss.* The measured wavelength-dependent absorption coefficient of the fluorinated polyurethane host was applied to all solid LSCs in simulations. Parasitic absorption losses in methanol in the reference design were considered to be negligible.

The Sankey diagram in Figure 3 illustrates what fraction of the incident power is lost to each mechanism in the case of Design 1. At the bottom of the diagram, it can be clearly seen that only a small fraction (0.2%) of the total incident power is absorbed by the  $\text{Nd}^{3+}$ -doped silica fiber. Although, the spectral mismatch loss and the non-absorption loss outweigh the other losses, these cannot be avoided while staying within the design scheme of using down-shifting dyes to pump the  ${}^4\text{G}_{5/2}$ - ${}^2\text{G}_{7/2}$   $\text{Nd}^{3+}$  absorption band. While a higher dye

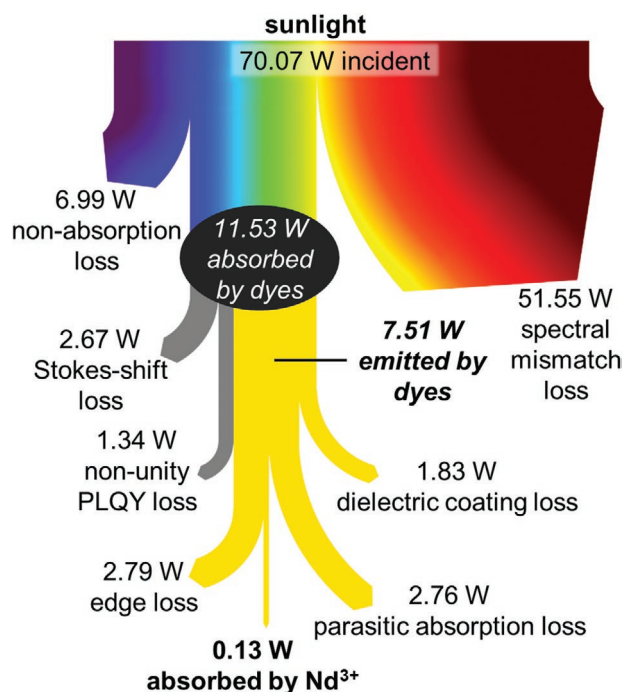


**Figure 3.** A Sankey diagram of the power balance in Design 1. The (external) spectral mismatch loss and the Stokes-shift loss are inevitable in the down-shifting scheme. The non-absorption loss is an optimization parameter, as the optical density not only determines the absorption of incident light, but also the spectrum of emitted light incident upon the silica fiber. Improvements would be possible with novel dyes possessing a narrower emission spectrum. The PLQY of the utilized dyes is exceptionally high, and the absorption coefficient of the host is small, thus there is only trivial improvement possible in the respective losses. Leaving aside new breakthrough materials, the only avoidable losses are the edge loss, and the dielectric coating loss, related to the reflectance of the surfaces of the light-trapping chamber.

concentration reduces the non-absorption losses, this would lead to a red shift of the spectrum incident on the silica fiber, and ultimately decrease the power in the  $\text{Nd}^{3+}$  absorption band (see Figure S4 in the Supporting Information). The dye concentration, or rather the single-pass peak optical density ( $\text{OD}_{\text{peak}}$ ), corresponding to the absorption peak of each individual dye, was optimized in simulations. For Design 1 and Design 2 an  $\text{OD}_{\text{peak}}$  of 1.4 and 0.8, with respect to the 1.5 mm thick LSC, was used for Y083 and O240, respectively. For Design 3 an  $\text{OD}_{\text{peak}}$  of 1.4 was used for Y083 in the LSC and an  $\text{OD}_{\text{peak}}$  of 3.2, with respect to the 5 mm wide ring LSC (see Methods below), was used for O240. The  $\text{OD}_{\text{peak}}$  of R6G in the reference design was 2.3 (corresponding to a R6G concentration of 0.3 mmol  $\text{L}^{-1}$ ).

Table 1 compares the simulated performance of the three solid LSC-based designs with the reference design. To validate the data, the 30 mW absorbed power by  $\text{Nd}^{3+}$  ions in the simulated reference design can be compared to experimentally determined small-signal gain of 1.9  $\text{km}^{-1}$  in the reference design.<sup>[27]</sup> The calculations are available in the Supporting Information (Section 3) and rely on the saturation intensity in the silica fiber. Two sources exist for saturation intensity, with a large discrepancy in the determined values ( $1.4 \times 10^8$   $\text{W m}^{-2}$ , and  $3.4 \times 10^8$   $\text{W m}^{-2}$ ).<sup>[27,29]</sup> The two values give a range of about 1  $\text{km}^{-1}$  to about 3  $\text{km}^{-1}$  for

**Table 1.** Summary of the power balance in the liquid-based reference design,<sup>[27]</sup> as well as in solid-state Designs 1, 2, and 3.

	Liquid LSC SPL		Solid-state LSC SPLs	
	Ref. design [W]	Design 1 [W]	Design 2 [W]	Design 3 [W]
Total incident power	70.07	70.07	70.07	70.07
Spectral mismatch loss	51.55	51.55	51.55	56.96
Non-absorption loss	9.37	6.99	6.99	5.56
Stokes-shift loss	1.53	2.67	2.62	1.62
Non-unity PLQY loss	1.28	1.34	1.21	0.66
<b>Power emitted by dyes</b>	<b>6.34</b>	<b>7.51</b>	<b>7.70</b>	<b>5.29</b>
Dielectric coating loss	4.55	1.83	1.29	1.30
Edge loss	1.77	2.79	4.36	1.82
Parasitic absorption loss	–	2.76	1.84	1.99
<b>Power absorbed by Nd<sup>3+</sup></b>	<b>0.03</b>	<b>0.13</b>	<b>0.21</b>	<b>0.18</b>

the small-signal gain related to an absorbed power of 30 mW, in good agreement to the experimentally determined small-signal gain.

The first key result, when comparing the performance and losses of all designs in Table 1, is that all solid-state designs outperform the reference design by a factor of 4–7 in terms of the power absorbed by Nd<sup>3+</sup> ions. This is a result of light only propagating by reflection on the dichroic coatings in the reference design. The dielectric coating losses are the highest in the reference. While in the solid-state designs, an air gap exists between the LSC and the dichroic coatings (see Figure 2b), additionally enabling propagation by TIR. Of the solid LSC designs, Design 3 shows the smallest internal absorption losses, with 3.4% of the dye emitted power being absorbed in the Nd<sup>3+</sup> ions compared to 1.7% and 2.7% for Designs 1 and 3, respectively. This indicates that the ring LSC achieves the best trapping of light in the vicinity of the silica fiber. However, to achieve this dual-stage cascade, only the higher-energy dye Y083 can be used for solar absorption in the central disc LSC. This leads to significantly higher spectral mismatch losses in Design 3 than the other designs and means that in total the simpler Design 2 still offers overall better performance. In general Design 2 shows the best performance in these simulations. In the next chapters it will become clear that placing the silica fiber inside the LSC is always superior to wrapping it around the outside. Furthermore, the largest internal loss in case of Design 2 is the edge loss. Of all internal loss mechanisms, the edge loss is the easiest to reduce.

In the following, possible reductions are discussed for each internal loss mechanism:

The *edge surface* is a cylindrical surface. The fabrication of high quality dielectric coating is challenging here, giving rise to the low reflectance of 45% at the edge.<sup>[27]</sup> Improvements can most certainly be achieved by employing highly reflective white paints, or aluminum coatings. For example, in Design 2 the edge loss accounts for more than half the internal losses. Thus, if the edge losses could be eliminated, it would roughly double the amount of emitted light flowing into the other channels, also doubling the power absorbed by the Nd<sup>3+</sup>.

*Dielectric coatings* are used on the front- and rear surface in the light-trapping chamber (Reflectance values given in the Supporting Information: Figure S5 and Figures S7–S10). Improvements are likely not possible, since dielectric surface are the most efficient at trapping light escaping from the LSC and allowing propagation towards the silica fiber. Here, white paints and metallic coatings are not suitable to replace the dielectric layers. White paints show high reflectance, but also scatter light, propagation over long distance is not possible. Similarly, long distance propagation is not possible with metal-based reflective cavities. With a reflectance of about 98% silver shows the highest reflectance in the visible range. However, for example when propagation at an angle of 60°, light impinges more than 50 times on the metallic surface while laterally traveling 100 mm in the 1.5 mm thick chamber. The available intensity after such a “short” distance is unacceptably reduced.

*Parasitic absorption* was introduced in simulations by applying the measured absorption coefficient of the polyurethane host of  $3.5 \times 10^{-3} \text{ cm}^{-1}$ , at 600 nm. A typical value for an LSC host material of high transparency.<sup>[38]</sup> Literature absorption coefficients for quartz at 600 nm vary from values as high as  $1.7 \times 10^{-2} \text{ cm}^{-1}$ ,<sup>[39]</sup> too as low as  $10^{-4} \text{ cm}^{-1}$ .<sup>[40]</sup> In this context the measured value is realistic, and significant improvements of the parasitic absorption are unlikely.

### 3.2. Optimum Silica Fiber Length

For the above comparison, a Nd<sup>3+</sup>-doped silica fiber length of 190 m was used in simulations to allow comparison with previous experimental work.<sup>[27]</sup> However, a key conclusion of the preceding section is that only a small fraction of the available light is absorbed by the silica fiber. The possibility for rectifying this – by increasing the amount of Nd<sup>3+</sup> in the cavity by introducing a longer silica fiber – is explored by simulation in the following. As long as the photon density in the silica fiber region remains constant, the absorption of light by Nd<sup>3+</sup> ions has a linear dependence on the fiber length. A longer silica fiber could be employed for higher gain. But, since the silica fiber itself effects the photon density in the systems by absorbing more of the emitted light (and altering the scattering) the photon density will be reduced as the fiber length increases and an optimum length must exist.

To compare the three solid designs with different lengths of fiber, the source diameter was kept constant at 300 mm and the packing density of the fiber (see Methods below) was kept constant as well. The radius of the fiber-containing portion of the design (see Methods below) was gradually increased with the fiber length to allow the fiber to just fit into the system at any given length. Thus, as the fiber length increases, so too does the outer radius of the structure. The change in radius as a function of fiber length is plotted in the Supporting Information (Figure S11). Since a constant power is incident in all simulations, the increasing volume means that the photon density in the light-trapping chamber will be decreased with increasing fiber length. These constraints allow a good comparison of the designs. But, an underestimation of the optimal length is likely, especially for Design 2, wherein increasing the radius of the dye-doped LSC for

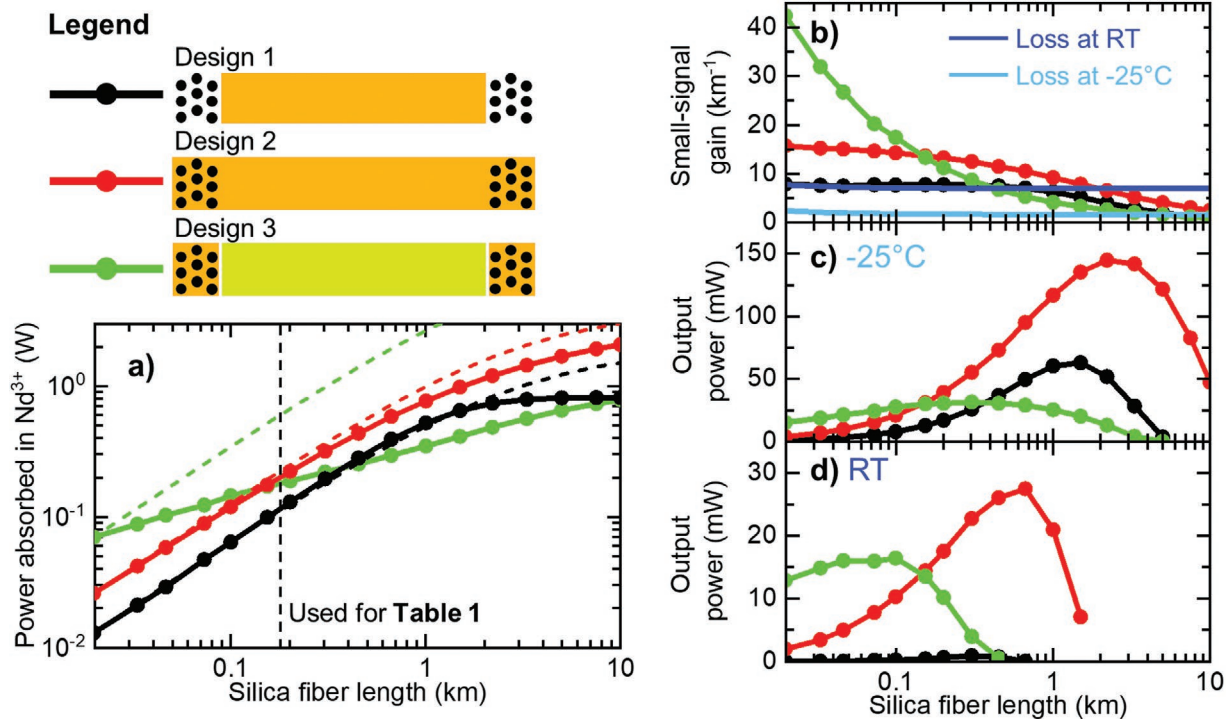


**Figure 4.** a) Simulation results for the three solid-state LSC Designs 1, Design 2, and Design 3 – indicating the power absorbed by  $\text{Nd}^{3+}$  ions as a function of the silica fiber length. The dashed lines show extrapolations (according to Equation (1)) assuming a linear dependency of absorbed power on the photon density in the light-trapping chamber. b) Calculated small-signal gain in Designs 1–3 based on the simulation result, as well as estimated losses at  $-25^\circ\text{C}$  and at room temperature (RT). c) Calculated output power at  $-25^\circ\text{C}$ . d) Calculated output power at RT.

longer fiber lengths, would obviously lead to an increase in the absorbed power.

Figure 4a presents the simulation results for the power absorbed in the  $\text{Nd}^{3+}$  ions as a function of the silica fiber length for the three designs under investigation. To understand the effect that silica fiber length has on the power density in the system, the expected power absorbed when taking the increase of the volume of the light-trapping chamber into account is shown as well. The dashed lines indicate the extrapolated absorbed power by  $\text{Nd}^{3+}$  ( $P_{\text{abs}}$ ) as a function silica fiber length ( $L$ ), assuming a linear relationship between the photon density and the chamber volume ( $V_c$ ):

$$P_{\text{abs}}(L) = \frac{P_{\text{abs}}(20\text{ m}) \cdot L(20\text{ m}) \cdot V_c(20\text{ m})}{L \cdot V_c(L)} \quad (1)$$

For a silica fiber length shorter than 1 km, both Design 1 and Design 2 exhibit a linear behavior. The simulated values and the simple extrapolation agree, indicating that the photon density is not significantly altered by the change in fiber length in this regime. When the length is further increased, the silica fiber starts strongly influencing the photon density in the chamber. Design 2 reaches 2 W of absorbed power at 10 km amounting to 26% of the light emitted by the dyes. In Design 1, the absorbed power does not surpass 0.8 W, due to light scattering introduced by the silica fiber. Light emitted from the LSC edge is scattered at fiber/air interfaces, limiting the penetration of the light into the fiber bundle. The primary consequence of this, in terms of limited SPL performance, is a

decrease in the total light absorption by the fiber. A secondary consequence is that the pumping is not uniform over the length of the fiber. Although this secondary consequence is not explicitly considered herein, it is also undesirable for lasing. The performance of Design 3 is decoupled from the chamber volume. The photon density in the ring LSC containing the silica fiber is far more relevant. The photon density in this ring is inversely related to the fiber length, as the volume of the ring scales linearly with fiber length. For short fiber lengths ( $< 100\text{ m}$ ) Design 3 outperforms the other designs, since the small volume of the ring LSC leads to high photon densities in the region of the fiber. This core strength of the design decreases as the ring LSC volume increases (with increasing fiber length) whereas the pump intensity from the disc LSC remains the same.

To consider what design and length of fiber is best, the first step is to determine the upper bounds for the fiber lengths based on round trip gain and loss considerations. Under continuous wave (CW) oscillation, the power in the laser cavity stays constant, the highest possible gain is given by the small-signal gain. The round-trip losses are the intrinsic loss in the silica fiber, and the miscellaneous losses at the resonator mirrors. Furthermore, it was found by Bisson et al.<sup>[29]</sup> that the thermal population of the lower laser level is non-negligible in the low-loss  $\text{Nd}^{3+}$ -doped silica fiber. This population of the lower laser level is a saturable loss; When the population of the upper and lower laser levels are equal, the loss vanishes and transparency is reached.<sup>[41]</sup> Thus, the gain coefficient ( $g_0$ ) in the system is given by

$$g_0(L, T) = \gamma_0(L) - \alpha_s(T) \quad (2)$$

where  $\gamma_0$  is the small-signal gain and  $\alpha_s$  the temperature-dependent saturable loss coefficient.  $L$  the length of the silica fiber and  $T$  the temperature. The bare minimum condition for lasing, not even considering the extraction of power, is:

$$\gamma_0 > \frac{A}{L} + \alpha_0 + a_s(T) \quad (3)$$

where  $\alpha_0$  is the intrinsic loss coefficient and  $A$  the mirror losses.  $\gamma_0$  can be estimated from the simulated power absorbed ( $P_{\text{abs}}$ ) using the relation  $\gamma_0(L) \approx (12 \text{ W}^{-1}) \times P_{\text{abs}}(L)/L$ . The relation is based on setting the simulated absorbed power in the reference design (30 mW, see section 3.1 above) equivalent to the measured  $1.9 \text{ km}^{-1}$  small-signal gain for this design.<sup>[27]</sup> The losses are also known from experiments, it is  $\alpha_0 = 6.9 \times 10^{-4} \text{ m}^{-1}$  (3 dB  $\text{km}^{-1}$ ),<sup>[9]</sup>  $A = 1.5\%$ ,<sup>[42]</sup> and  $\alpha_s(-25 \text{ }^\circ\text{C}) = 9.5 \times 10^{-4} \text{ m}^{-1}$  ( $\alpha_s(23 \text{ }^\circ\text{C}) = 6.3 \times 10^{-3} \text{ m}^{-1}$ ).<sup>[29]</sup> The calculated small-signal gain coefficient for each design as a function of the silica fiber length is shown in Figure 4b, along with the loss per unit length (right-hand side of Equation (3)) for  $-25 \text{ }^\circ\text{C}$  and room temperature ( $23 \text{ }^\circ\text{C}$ ). At a temperature of  $-25 \text{ }^\circ\text{C}$ , the small-signal gain coefficient is larger than all losses, in all designs, for many kilometers of silica fiber length. However, it is immediately apparent that Design 1 is not suitable for lasing at room temperature. Lasing at room temperature should only be possible in Design 2, up to a silica fiber length of about 1 km, and in Design 3, up to a length of about 200 m.

The above analysis is qualitatively instructive but, to more quantitatively consider the optimum length for fiber length, the output power of the laser as a function of fiber length must be estimated. Naturally, the output power of the laser also depends on the choice of the reflectivity for the output coupler, and the saturation intensity. However, it is possible to calculate the output power ( $P_{\text{opt}}$ ) of the laser at the optimum output coupler reflectivity by:<sup>[41]</sup>

$$P_{\text{opt}} = g_0 I_s V \left(1 - \sqrt{(\alpha_0 + A/L) / g_0}\right)^2 \quad (4)$$

where  $I_s$  is the saturation intensity,  $V$  is the gain volume. The saturation intensity for the fibers used has previously been extracted as  $I_s = 1.4 \times 10^8 \text{ W m}^{-2}$ .<sup>[27]</sup> The volume can be calculated based on the  $16 \text{ } \mu\text{m}$   $\text{Nd}^{3+}$ -doped core diameter, yielding  $V(L) = L \times 2.01 \times 10^{-10} \text{ m}^2$ . Figure 4c demonstrates the output power at a temperature of  $-25 \text{ }^\circ\text{C}$ . For a length of 190 m Design 2 exhibits the highest output power, with a value of 39 mW being a factor of 30 higher than the power output in the reference design (1.3 mW). With the low saturable loss of the fiber at  $-25 \text{ }^\circ\text{C}$ , maximum laser powers are achieved at relatively long fiber lengths. Since Design 2 possesses the highest small-signal gain for these long lengths, it is particularly attractive, with the 145 mW the maximum output power being more than double that of any of the other two designs. Due to its large ring LSC volume, Design 3 is the least useful when it comes to long silica fiber lengths.

At room temperature, much higher saturable losses are encountered in the  $\text{Nd}^{3+}$ -doped silica fiber, the situation

becomes significantly different. As is illustrated in Figure 4d, under this condition, a shorter fiber length is favored. Here, is when Design 3 becomes more attractive, due to its high small-signal gain coefficient for short silica fiber length. However, with a calculated maximum output power of 16 mW at a length of about 100 m, Design 3 still performs worse than Design 2, with a maximum output power of 28 mW at a length of 600 m.

Based on the currently available data Design 2 is clearly the best design. Design 3 has the potential to outperform Design 2 in case of high silica fiber losses, but even at room temperature this was not achieved. A critical criterion for the performance of Design 3 is the volume of the ring LSC, directly related to the packing density of the silica fiber. Thus, it is a question of technical feasibility to what extent the volume could further be reduced, while maintaining the same silica fiber length. In general, with a spacing of  $200 \text{ } \mu\text{m}$  between the cores in the fiber coil (see Methods below), the packing density was chosen rather low in these simulations. A higher packing density, also enabled for example by reducing the diameter of the silica fiber cladding, would allow coiling a silica fiber of a specific length in smaller volume. A further possibility to increase the photon density in Design 2, is decreasing the thickness of the light-trapping chamber.

### 3.3. Scattering

Scattering critically influences the propagation of light through the light-trapping chamber. Scattering is unavoidable in Design 1, as the fiber-air interface is an inherent part of the design. However, this scattering was deliberately reduced in Designs 2 and 3 by choosing a host material with a refractive index similar to that of silica. Just like reabsorption (see Figure 2c), scattering leads to light escaping from the LSC, exhibited as a disruption in TIR. However, the employed dielectric coatings trap this light escaping from the LSC. Thus, scattering is less important when employing an efficient light-trapping chamber. *Vice versa*, scattering is important when removing the dielectric coatings. The dielectric coatings have two important disadvantages. First, the dielectric coatings are by far the most expensive part of the system. Second, the transmittance of light of a dichroic coating is sensitive to the incidence angle. Only normal incident light was considered in this work, while diffuse light plays a significant role in terrestrial use, and the incidence angle of the sun changes throughout the day. Under these conditions, the non-absorption loss of the dichroic mirror are much higher, in comparison to an uncoated air-SiO<sub>2</sub> interface (see Figure S6 in the Supporting Information). With these disadvantages in mind, the importance of scattering in Design 2 and 3 is further investigated in an SPL with and without dielectric coatings.

For the following discussion, the scattering coefficient in the host material was varied. A scattering coefficient of  $10^{-1} \text{ cm}^{-1}$  was implemented for the doped solid-state host in all simulations discussed until now. The coefficient was based on measurements of the specular transmittance and absorptance in thick samples. Since the exact angular distribution of scattered light was unknown, isotropic scattering was assumed in all simulations. This deliberate over-estimation was employed to compensate for neglecting the effects of surface scattering (it was assumed that all surfaces are perfectly flat).



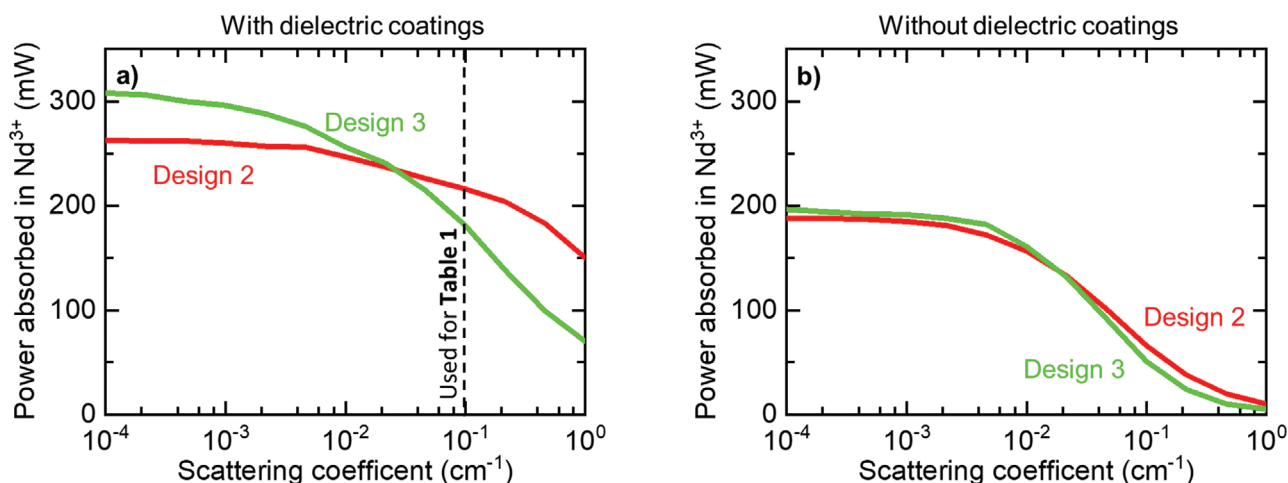


**Figure 5.** Power absorbed by  $\text{Nd}^{3+}$  ions as a function of the scattering coefficient in the host material. a) Case when the LSC and silica fiber are placed in a light-trapping chamber based on dielectric coatings on all sides. b) Case when the LSC and silica fiber are placed in a chamber of identical dimensions, but with aluminum coatings on the rear and edge surface of the chamber, and without a dichroic front mirror on the fused silica cover.

Figure 5 shows the power absorbed by  $\text{Nd}^{3+}$  ions as a function of the volume scattering coefficient of the host material for Design 2 and 3. A 190 m long silica fiber was used in these simulations. The scattering coefficient was varied over 4 orders of magnitude from  $10^{-4} \text{ cm}^{-1}$  to  $10^0 \text{ cm}^{-1}$ . Values below  $10^{-4} \text{ cm}^{-1}$  have been measured for the common LSC host material PMMA,<sup>[43]</sup> but the refractive index of PMMA is higher than that of silica, leading to more scattering at the interface. Figure 5a shows the simulation results when including the dielectric coatings. Scattering has a negligible effect on the performance of Design 2 in this case, since the dielectric coatings trap the light escaping from the LSC. Scattering is more relevant to Design 3, since the design targets high photon densities in the ring LSC of small volume. Scattering reduces the photon density in the ring LSC. When reducing the scattering coefficient below a value of  $3 \times 10^{-2} \text{ cm}^{-1}$  in simulations, Design 3 outperforms Design 2 (for a silica fiber length of 190 m).

Figure 5b shows the absorbed power when removing the dielectric coatings. The dichroic front surface coating was fully removed, and instead of the dielectric coatings on the rear surface an aluminum coating (exhibiting a reflectance of 90%) was employed. The aluminum coating was used for the edge surface of the light-trapping chamber as well. The air gaps between the coatings and the LSC (see Figure 2c,d) were maintained. Now, the scattering of light becomes highly relevant. In case of strong scattering, light escapes from the LSC and is lost. Little power reaches the silica fiber. However, for a scattering coefficient smaller than about  $10^{-2} \text{ cm}^{-1}$  – equivalent to a mean free path length of 100 cm, about 3 times the LSC diameter – the power absorbed by  $\text{Nd}^{3+}$  ions reaches levels comparable to the case with the light-trapping chamber. This demonstrates that when scattering is reduced inside the LSC (and at all interfaces), there is no need for employing dielectric coatings. Or expressed in another way, in case of low scattering, the light-trapping chamber must be of exceptional quality to significantly increase the performance of the SPL (e.g., show lower edge reflectance than what is currently achieved). In future work, when translating the SPL performance from direct to diffuse lighting conditions, this consideration will be even more important for determining the best possible design.

## 4. Conclusions

In this work, implementations of 300 mm diameter solid-state LSCs to pump a  $\text{Nd}^{3+}$ -doped silica fiber in an SPL system were investigated by ray-tracing simulations and modeling. The LSC and the silica fiber are to be placed in a light-trapping chamber (equipped with dielectric coatings) to counteract the low absorption of light transversally passing through the doped core of the silica fiber. Three designs for placing the silica fiber with respect to the LSC are introduced and evaluated. In Design 1, the silica fiber is wrapped around the LSC in air. In Design 2, the silica fiber is placed inside the LSC. In Design 3, the silica fiber is placed in a thin separate ring LSC around a central disc LSC.

The simulated geometries closely match the functional liquid-based SPL fabricated by Masuda et al.<sup>[27]</sup> This reference SPL was also used to validate the simulation results via a comparison to experimental data. While the liquid-based SPL relies solely on reflection by the dielectric coating of the surrounding chamber to concentrate light, the here investigated solid designs additionally make use of TIR. All three solid-state LSC designs outperformed the liquid reference by at least a factor of 4 in terms of absorbed power, while employing a silica fiber of identical length, a light-trapping chamber of identical dimensions, and identical illumination conditions. Not only does this significant increase allow higher laser output powers, by up to a factor of 30, but estimations also indicate that Design 2 and Design 3 should be operable at room temperature, while the liquid-based system needed to be cooled to below  $-25 \text{ }^\circ\text{C}$  to reduce round trip losses.

Calculations were performed to determine the optimum silica fiber length for the assorted designs. The optimum length, and with it the maximum possible laser output power, is determined by the (temperature-dependent) fiber losses. The higher the losses, the shorter the optimum fiber length, since the small-signal gain coefficient reduces with the length. Design 2 shows the least reduction in the small-signal gain coefficient when increasing the silica fiber length. Thus, it is the best design when the intrinsic losses are small at low temperatures. For a silica fiber length of about 3 km a laser output power of 145 mW was calculated, a more than 100-fold increase

from the 1.3 mW measured for the liquid-based SPL. At higher temperatures, with higher intrinsic losses, the optimum silica fiber length is reduced. Thus, at higher temperatures, Design 3, with the fiber in a ring LSC, becomes a more attractive design. However, based on the parameters used here even at room temperature Design 2 still shows the best performance.

A further finding is the importance of light scattering in the systems. For example, the scattering of light on the curved silica fiber surface can play a key role in reducing the small-signal gain when increasing the silica fiber length. Scattering in general lets TIR trapped light escape. Scattering in the ring LSC in Design 3 is thus highly critically for the performance. When designing a system with little scattering it is possible to efficiently operate the system without employing a light-trapping chamber based on dielectric coatings.

The results presented here indicate that LSC-based SPLs with hundreds of mW output power should be a feasible next target. Such power levels are more consistent with applications in communication systems rather than, e.g., power transmission. However, this technology is very much at a fledgling stage and the potential to further optimize SPL systems, based on the scalability of LSCs, is significant. Of the investigated solid-state designs, Design 2 with the silica fiber inside the LSC is the most promising. Future experiments should focus on this approach. From a technical point of view, optical contact between the silica fiber and the LSC is important. It is thus not necessary to fabricate the LSC around the silica fiber, but the silica fiber could be attached to the LSC using a different host material in optical contact to the LSC. Based on these results, experimental realization of improved SPLs based on LSCs should be feasible.

## 5. Methods

### 5.1. Measured Parameters

#### 5.1.1. Fluorinated Polyurethane Host

The fluorinated polyurethane host was prepared using the polyol Lumiflon LF 910LM (AGC Chemicals) and isocyanate Desmodur ultra N 3300 (Covestro AG). The two components were mixed (NCO/OH = 1) by magnetic stirring. When needed, the dyes Lumogen F O240 (BASF) and Lumogen F Y083

(BASF) were dissolved in chloroform (Sigma Aldrich) at  $1 \text{ g L}^{-1}$  and added to the mixture. After casting, the layers were placed in a furnace at  $80 \text{ }^\circ\text{C}$  for 24 h to evaporate solvents and accelerate the polyurethane reaction.

The absorption and scattering coefficients of the polyurethane host were determined from absorbance and specular transmittance measurements performed with a spectrophotometer (Lambda 950, Perkin Elmer). The corresponding calculations and the wavelength-dependent data implemented in simulations are available in the Supporting Information (Figure S2). The refractive index was measured using a commercial prism coupler (Model 2010/M, Metricon). At 637 nm a refractive index of 1.47 was determined.

#### 5.1.2. Dye Excitation and Emission Spectra

The excitation and emission spectra of the used dyes were determined using a commercial fluorescent spectrometer (Cary Eclipse, Agilent). For the measurements, polyurethane layers containing one of the dyes (Lumogen F O240 or Lumogen F Y083) were cast on glass substrates. Low dye concentrations (10 ppm) were used to obtain the molecular emission spectra (with negligible reabsorption). High dye concentrations (1000 ppm) were used to obtain detailed data on the absorption tail in the excitation spectrum, relevant for accurately simulating the red shift of the edge emission spectrum. Similarly, a low ( $10^{-2} \text{ g L}^{-1}$ ) and a high concentration ( $1 \text{ g L}^{-1}$ ) Rhodamine 6G (Sigma Aldrich) in methanol (Sigma Aldrich) were prepared. The measured spectra for all dyes are available in the Supporting Information (Figure S3).

### 5.2. Simulation Environment

Simulations were performed in LightTools (Synopsis), a program based on ray tracing. In the simulation environment, rays were emitted from a cylindrical source onto the front surface of the system at normal incidence (see Figure 6). The wavelengths were assigned to each ray based on the probability distribution of the AM1.5g spectrum,<sup>[32]</sup> and the incident power was normalized to  $1000 \text{ W m}^{-2}$ . To increase the comparability of all simulations a source diameter 300 mm

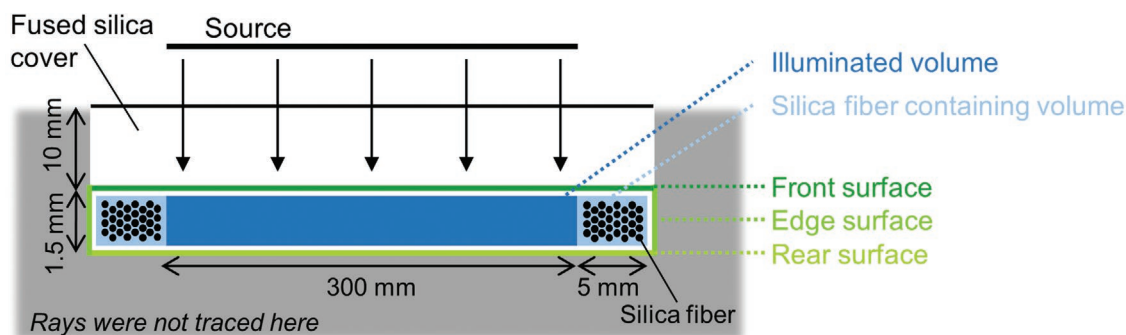


**Figure 6.** Illustration of the simulation environment. The dimension of the source, the dimensions of the “illuminated volume” and the position of the silica fiber was kept constant in all simulations. For simulating the assorted designs, only the reflectance of the front- and rear surface, and the dye doping and host material of the “illuminated volume” and “silica fiber containing volume” were changed.

was used, keeping the incident power constant at a value 70.07 W. Light entered the light-trapping chamber through a 10 mm thick slab with optical properties to represent fused silica (refractive index data used from literature).<sup>[35]</sup> The silica fiber was implemented with multiple toroids. Each toroid consisted of an absorption-free outer toroid of 125 μm diameter, representing the fiber cladding, and an inner toroid of 16 μm diameter, representing the fiber core (closely matching the properties of the silica fiber employed in the reference design, supplied by Furukawa Denko Corp). The refractive index of fused silica, available in literature,<sup>[35]</sup> was used in both cases. In cross-section the toroids were arranged in a hexagonal lattice (see Figure 6), with a lattice constant of 200 μm. Modeling of a continuous fiber was not necessary, as the key figure of merit is the power absorbed in the fiber core (absorption coefficient available in Figure 1d).

Four components of the simulation environment (front surface, rear surface, illuminated volume, and silica fiber containing volume – see Figure 6) were adapted for simulating the three solid-state designs and the liquid reference design. The reflectance of the two surfaces, front surface and rear surface, were optimized for each design. TFCalc (Software Spectra, Inc.) was used to optimize the thickness of 80 layers of SiO<sub>2</sub> and TiO<sub>2</sub>, and the calculated reflectance was implemented in simulations. The optimization parameters and the reflectance values are available in the Supporting Information (Figure S5 and Figure S7–S10). The edge reflectance was 45% in all simulations. The illuminated volume had a diameter of 300 mm in all simulations, the host material and the contained dyes of this volume were adapted. The width of silica fiber containing volume was changed, to just contain the silica fiber at any given length (e.g., 5 mm for 190 m silica fiber length), the host material and the contained dyes of this volume were adapted. When necessary an air gap of 10 μm was included. A detailed list of the properties used to model each design is available in the Supporting Information (Table S1).

## Supporting Information

Supporting Information is available from the Wiley Online Library or from the author.

## Acknowledgements

The authors thank the Helmholtz Association (Helmholtz Energy Materials Foundry and B.S.R. recruitment initiative) for funding. B.S.R. thanks the Helmholtz Program MTET for financial support (Topic 1 Wind Energy & Photovoltaics).

Open access funding enabled and organized by Projekt DEAL.

## Conflict of Interest

The authors declare no conflict of interest.

## Data Availability Statement

Research data are not shared.

## Keywords

luminescent solar concentrators, ray tracing, solar-pumped lasers

Received: March 8, 2021

Revised: March 18, 2021

Published online: May 6, 2021

- [1] Z. J. Kiss, H. R. Lewis, R. C. D. Jr., *Appl. Phys. Lett.* **1963**, 2, 93.
- [2] T. Kato, H. Ito, K. Hasegawa, T. Ichikawa, A. Ikesue, S. Mizuno, Y. Takeda, A. Ichiki, T. Motohiro, *Jpn. J. Appl. Phys.* **2019**, 58, 062007.
- [3] C. J. C. Smyth, S. Mirkhanov, A. H. Quarterman, K. G. Wilcox, *Appl. Opt.* **2018**, 57, 4008.
- [4] Y. Suzuki, H. Ito, T. Kato, L. T. A. Phuc, K. Watanabe, H. Terazawa, K. Hasegawa, T. Ichikawa, S. Mizuno, A. Ichiki, S. Takimoto, A. Ikesue, Y. Takeda, T. Motohiro, *Sol. Energy* **2019**, 177, 440.
- [5] D. Liang, C. R. Vistas, J. Almeida, B. D. Tibúrcio, D. Garcia, *Sol. Energy Mater. Sol. Cells* **2019**, 192, 147.
- [6] S. Payziyev, K. Makhmudov, *Opt. Commun.* **2016**, 380, 57.
- [7] B. D. Tibúrcio, D. Liang, J. Almeida, D. Garcia, C. R. Vistas, P. J. Morais, *Opt. Commun.* **2020**, 460, 125156.
- [8] J. Almeida, D. Liang, E. Guillot, *Opt. Laser Technol.* **2012**, 44, 2115.
- [9] T. Masuda, M. Iyoda, Y. Yasumatsu, M. Endo, *Opt. Lett.* **2017**, 42, 3427.
- [10] S. Mehellou, D. Liang, J. Almeida, R. Bouadjemine, C. R. Vistas, E. Guillot, F. Rehouma, *Sol. Energy* **2017**, 155, 1059.
- [11] B. D. Tibúrcio, D. Liang, J. Almeida, D. Garcia, C. R. Vistas, *Appl. Opt.* **2019**, 58, 3438.
- [12] T. H. Dinh, T. Ohkubo, T. Yabe, H. Kuboyama, *Opt. Lett.* **2012**, 37, 2670.
- [13] Z. Guan, C. Zhao, J. Li, D. He, H. Zhang, *Opt. Laser Technol.* **2018**, 107, 158.
- [14] D. Liang, C. R. Vistas, B. D. Tibúrcio, J. Almeida, *Sol. Energy Mater. Sol. Cells* **2018**, 185, 75.
- [15] H. Costa, J. Almeida, D. Liang, D. Garcia, M. Catela, B. D. Tibúrcio, C. R. Vistas, *Opt. Eng.* **2020**, 59, 086103.
- [16] T. Yabe, S. Uchida, K. Ikuta, K. Yoshida, C. Baasandash, M. S. Mohamed, Y. Sakurai, Y. Ogata, M. Tuji, Y. Mori, Y. Satoh, T. Ohkubo, M. Murahara, A. Ikesue, M. Nakatsuka, T. Saiki, S. Motokoshi, C. Yamanaka, *Appl. Phys. Lett.* **2006**, 89, 261107.
- [17] N. Yamada, T. Ito, H. Ito, T. Motohiro, Y. Takeda, *Jpn. J. Appl. Phys.* **2018**, 57, 08RF07.
- [18] D. Goto, H. Yoshida, H. Suzuki, K. Kisara, K. Ohashi, Y. Arimoto, presented at *Int. Conf. on Space Optical Systems and Applications (ICSOS 2014)*, Kobe, Japan **2014**, paper S5-2.
- [19] Y. K. Bae, *Phys. Procedia* **2012**, 38, 253.
- [20] R. J. De Young, G. D. Walberg, E. J. Conway, L. W. Jones, A NASA high-power space-based laser research and applications program, NASA **1983**, 19830018929.
- [21] Z. Guan, C. M. Zhao, S. H. Yang, Y. Wang, J. Y. Ke, H. Y. Zhang, *Laser Phys. Lett.* **2017**, 14, 055804.
- [22] T. Motohiro, Y. Takeda, H. Ito, K. Hasegawa, A. Ikesue, T. Ichikawa, K. Higuchi, A. Ichiki, S. Mizuno, T. Ito, N. Yamada, H. N. Luitel, T. Kajino, H. Terazawa, S. Takimoto, K. Watanabe, *Jpn. J. Appl. Phys.* **2017**, 56, 08MA07.
- [23] P. D. Reusswig, S. Nechayev, J. M. Scherer, G. W. Hwang, M. G. Bawendi, M. A. Baldo, C. Rotschild, *Sci. Rep.* **2015**, 5, 14758.
- [24] W. H. Weber, J. Lambe, *Appl. Opt.* **1976**, 15, 2299.
- [25] A. Goetzberger, W. Greube, *Appl. Phys.* **1977**, 14, 123.
- [26] W. H. Press, *Nature* **1976**, 264, 734.
- [27] T. Masuda, M. Iyoda, Y. Yasumatsu, S. Dottermusch, I. A. Howard, B. S. Richards, J.-F. Bisson, M. Endo, *Commun. Phys.* **2020**, 3, 60.
- [28] T. Masuda, Y. Zhang, C. Ding, F. Liu, K. Sasaki, Q. Shen, M. Endo, *J. Appl. Phys.* **2020**, 127, 243104.

- [29] J.-F. Bisson, M. Iyoda, Y. Yasumatsu, M. Endo, T. Masuda, *J. Opt. Soc. Am. B* **2019**, 36, 736.
- [30] M. G. Debije, P. P. C. Verbunt, *Adv. Energ. Mater.* **2012**, 2, 12.
- [31] R. A. S. Ferreira, S. F. H. Correia, A. Monguzzi, X. Liu, F. Meinardi, *Mater. Today* **2020**, 33, 105.
- [32] National Renewable Energy Laboratory, *Reference Air Mass 1.5 Spectra*, [www.nrel.gov/grid/solar-resource/spectra-am1.5.html](http://www.nrel.gov/grid/solar-resource/spectra-am1.5.html) (accessed: October 2020).
- [33] B. J. Ainslie, S. P. Craig, S. T. Davey, B. Wakefield, *Mater. Lett.* **1988**, 6, 139.
- [34] S. Nechayev, P. D. Reusswig, M. A. Baldo, C. Rotschild, *Sci. Rep.* **2016**, 6, 38576.
- [35] I. H. Malitson, *J. Opt. Soc. Am.* **1965**, 55, 1205.
- [36] M. Fischer, J. Georges, *Chem. Phys. Lett.* **1996**, 260, 115.
- [37] L. R. Wilson, B. S. Richards, *Appl. Opt.* **2009**, 48, 212.
- [38] F. Meinardi, F. Bruni, S. Brovelli, *Nat. Rev. Mater.* **2017**, 2, 17072.
- [39] M. A. Khashan, A. Y. Nassif, *Opt. Commun.* **2001**, 188, 129.
- [40] J. A. Harrington, B. L. Bobbs, M. Braunstein, R. K. Kim, R. Stearns, R. Braunstein, *Appl. Opt.* **1978**, 17, 1541.
- [41] W. Koechner, *Solid-State Laser Engineering*, Springer, Heidelberg, Germany **1999**.
- [42] T. Masuda, M. Iyoda, Y. Yasumatsu, M. Endo, *Rev. Sci. Instrum.* **2017**, 88, 053112.
- [43] K. Koike, Q. Du, S. Nishino, Y. Koike, *Polymer* **2014**, 55, 878.